White-light Continuum Observation of the Off-limb Loops of the SOL2017-09-10 X8.2 Flare: Temporal and Spatial Variations

Junwei Zhao[1], Wei Liu[2,3], and Jean-Claude Vial[4]

ABSTRACT

Observations of the Sun's off-limb white-light (WL) flares offer rare opportunities to study the energy release and transport mechanisms in flare loops. One of the best such events was SOL2017-09-10, an X8.2 flare that occurred near the Sun's west limb on 2017 September 10 and produced a WL loop system lasting more than 60 minutes and reaching an altitude higher than 30 Mm. The event was well observed by a suite of ground- and space-based instruments, including the *Solar Dynamics Observatory*/Helioseismic and Magnetic Imager (*SDO*/HMI) that captured its off-limb loops in WL continuum near Fe I 6173 Å, and the Atmospheric Imager Assembly (*SDO*/AIA) that observed its ultraviolet (UV) and extreme-ultraviolet (EUV) counterparts. We found quasi-periodic pulsations in the WL and UV emissions at the flare loop-top with a period around 8.0 min. Each pulsation appears to have an EUV counterpart that occurs earlier in time and higher in altitude. Despite many similarities in the WL and UV images and light curves, the WL flux at the loop-top continues to grow for about 16 minutes while the UV fluxes gradually decay. We discuss the implication of these unprecedented observations on the understanding of the enigmatic off-limb WL flare emission mechanisms.

Subject headings: Sun: activity — Sun: corona — Sun: flares — oscillations — UV radiation

1. Introduction

White-light flares (WLFs; Hudson et al. 2006; Hudson 2011) are rare flaring events that cause continuum emission in excess of the photospheric background. Off-limb WLFs, with flare-loop

[1]W. W. Hansen Experimental Physics Laboratory, Stanford University, Stanford, CA 94305-4085, USA

[2]Lockheed Martin Solar and Astrophysics Laboratory, Palo Alto, CA94304, USA

[3]Bay Area Environmental Research Institute, NASA Research Park, Moffett Field, CA 94035, USA

[4]Institut d'Astrophysique Spatiale, Université Paris-Saclay, C.N.R.S., Batiment 121, ORSAY 91405, France

brightening observed in white light (WL) beyond the solar limb, are even rarer with only a few cases reported (e.g., Hiei et al. 1992; Martínez Oliveros et al. 2014). Three off-limb WLFs were so far observed in the continuum near Fe I 6173 Å by the Helioseismic and Magnetic Imager (HMI; Scherrer et al. 2012; Schou et al. 2012) onboard the spacecraft *Solar Dynamics Observatory* (*SDO*; Pesnell et al. 2012), i.e., SOL2013-05-13T02:16 (X1.7), SOL2013-05-13T16:01 (X2.8), and SOL2017-09-10T15:35 (X8.2). These observations offered unprecedented opportunities for solar physicists to study properties of WLFs that are otherwise impossible: e.g., Martínez Oliveros et al. (2014) compared the WL brightening sources with those observed in extreme ultraviolet (EUV) and soft X-ray; Saint-Hilaire et al. (2014) analyzed the linear polarization observed in the WL flare loops; and Heinzel et al. (2017) studied emission mechanisms of the WL off the solar limb.

One popular phenomenon that is associated with solar flaring events and has been widely studied by various authors is quasi-periodic pulsations (QPPs) in the time-dependent intensity curves observed in different wavelengths during flares (Nakariakov & Melnikov 2009; Van Doorsselaere et al. 2016). This phenomenon, with a repeating period of a few seconds to a few minutes, has been observed almost across all the electromagnetic spectrum, such as in γ-rays (Nakariakov et al. 2010), EUV and soft X-rays (e.g., Dennis et al. 2017; Dominique et al. 2018), chromospheric lines (e.g., Brosius et al. 2016; Tian et al. 2016), and also in radio bursts (e.g., Li et al. 2015). Due to the rare observation of WLFs, no known QPP has yet been reported in white light. The physical mechanism for the generation of QPP is not very clear, but it is believed that this phenomenon is either due to the characteristics of the flaring loops that exhibit magnetohydrodynamic (MHD) oscillations at the flaring sites or MHD waves passing through the flaring loops (e.g., Nakariakov & Melnikov 2009), or due to the quasi-periodic magnetic reconnection and energy release that power the intensity enhancements of the spectrum lines (e.g., Murray et al. 2009).

The X8.2 limb flare of 2017 September 10 (SOL2017-09-10T15:35), whose loops rose right above the Sun's west limb and which was well observed by a suite of ground- and space-based instruments, has been studied from many different perspectives to tackle various physics problems related to flare dynamics and energy releases. For example, using EUV observations Warren et al. (2018) studied the formation and evolution of the current sheet following the eruption; Coupling hard X-ray and ground-based radio observations, Gary et al. (2018) studied the evolving spatial and energy distribution of high-energy electrons in the flaring region; Coupling with *GOES* X-ray and EUV observations, Hayes et al. (2019) found QPPs with periods of about 65 s and 150 s; Using the *SDO*/HMI's WL observations, Jejčič et al. (2018) modeled the physical conditions inside the flare loops and explored the WL emission mechanisms; Heinzel et al. (2020) identified signatures of He continuum in the cool flare loops; Using Ca II Stokes components observed by the Swedish 1m Solar Telescope, Kuridze et al. (2019) reported a strong magnetic field of 350 G at the flare's loop-top; Using microwave observations, Fleishman et al. (2020) estimated that the

coronal magnetic field in the flaring loops decayed with a rate of ~ 5 G s^{-1} during the flare, and Yu et al. (2020) analyzed the bidirectional outflows from the magnetic reconnection sites.

In this Letter, combining simultaneous observations of the SOL2017-09-10 flare obtained in the *SDO*/HMI's continuum intensity and *SDO*/AIA's (Atmospheric Imaging Assembly; Lemen et al. 2012) ultraviolet (UV) and EUV observations, along with data from the *Geostationary Operational Environmental Satellite* (*GOES*) and *Reuven Ramaty High Energy Solar Spectroscopic Imager* (*RHESSI*; Lin et al. 2002), we analyze the temporal and spatial variations of the brightening observed in different wavelength channels, as well as the QPPs in all these channels. It is believed that these unprecedented simultaneous observations in different wavelength channels offer us a rare opportunity to understand the emission mechanism of white light, heat dissipation process, and energy releases during the flare. This Letter is organized as follows: we introduce observations in Section 2, present our analysis and results in Section 3, and discuss our results in Section 4.

2. Observations

The *SDO*/HMI uses Fe I 6173 Å line to observe the Sun with $1''$ spatial resolution and 45 sec temporal cadence, and provides full-disk continuum intensity data, along with Doppler velocity and magnetic field. The field of view of *SDO*/HMI is nominally $45''$ wider than the photospheric solar disk, allowing detection of features bright in visible light immediately beyond the solar limb. The SOL2017-09-10 X8.2 flare started at approximately 15:35 UT in NOAA Active Region 12673, when most of the active region rotated around the west limb into far side of the Sun. The sudden brightening at the footpoints of the flare in the chromosphere and the rise of the bright flare loops, up to about $40''$ above the limb, were observed by the *SDO*/HMI in its continuum intensity, i.e., white light. As shown in Figure 1 and its associated online animation, the flare loops become visible above the limb at around 16:03:00 UT. Its loop-top brightness gradually enhances with the increase of height, reaching an intensity maximum at about 16:12:00 UT when the *SDO*/AIA's UV channels also reach their respective maxima (Cf. Figure 4b). While continuing to rise in height, the WL intensity drops for about 5 min, and then starts to enhance again, reaching a even brighter maximum at about 16:27:45 UT. The WL brightening of the flare loops then gradually fade away, lasting a total of about 70 min.

The flare was also observed in all the *SDO*/AIA wavelength channels. However, due to the powerful intensity of this flare, a number of AIA channels either saturated near and during the peak of the flare, mostly at the location of the loop-top, or had irregular exposure times in order not to saturate the observations. The data from those channels with irregular exposure times may still be useful for some types of analyses, but cannot be used in this analysis, which focuses on temporal

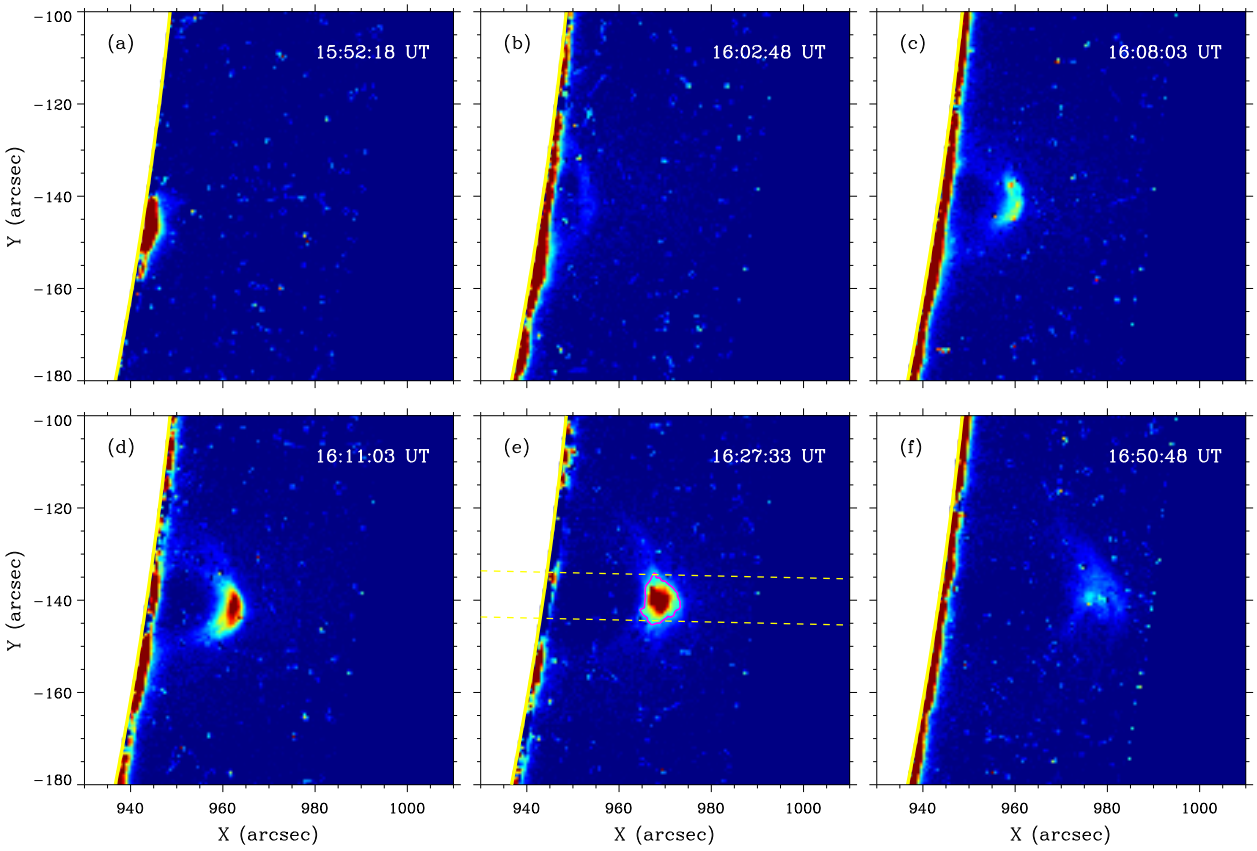

Fig. 1.— Selected white-light images from the *SDO*/HMI observations show temporal evolution of the flare's off-limb loops, after a long-time-averaged pre-flare background is removed. White area on the left side of each panel indicates the Sun's photospheric disk and limb. Yellow dashed lines in panel (e) delimit the area inside which intensities are integrated for further analysis, and the magenta contour showing the WL loop-top is used in Figure 2c for a location comparison. (An animation showing the entire sequence of the event is available online, with a total running time of 7 seconds.)

variations of the loop-top intensity and is sensitive to the alteration of exposure times. This leaves only observations from the wavelengths of two UV channels (1700 Å and 1600 Å) and two EUV channels (335 Å and 304 Å) useful for the analysis in this study. According to Lemen et al. (2012), the UV channel 1700 Å (1600 Å) is sensitive to the temperature of $10^{3.7}$ K ($10^{5.0}$ K) corresponding to the upper photosphere (the upper photosphere and transition region), the EUV channel 304 Å (335 Å) is sensitive to the temperature of $10^{4.7}$ K ($10^{6.4}$ K) corresponding to the chromosphere and transition region (active region corona). However, it must be stressed that these properties of different channels are assessed mostly for on-disk observations, and may not strictly apply to the off-limb observations. Figure 2 shows key snapshots of the flare loops for some wavelengths,

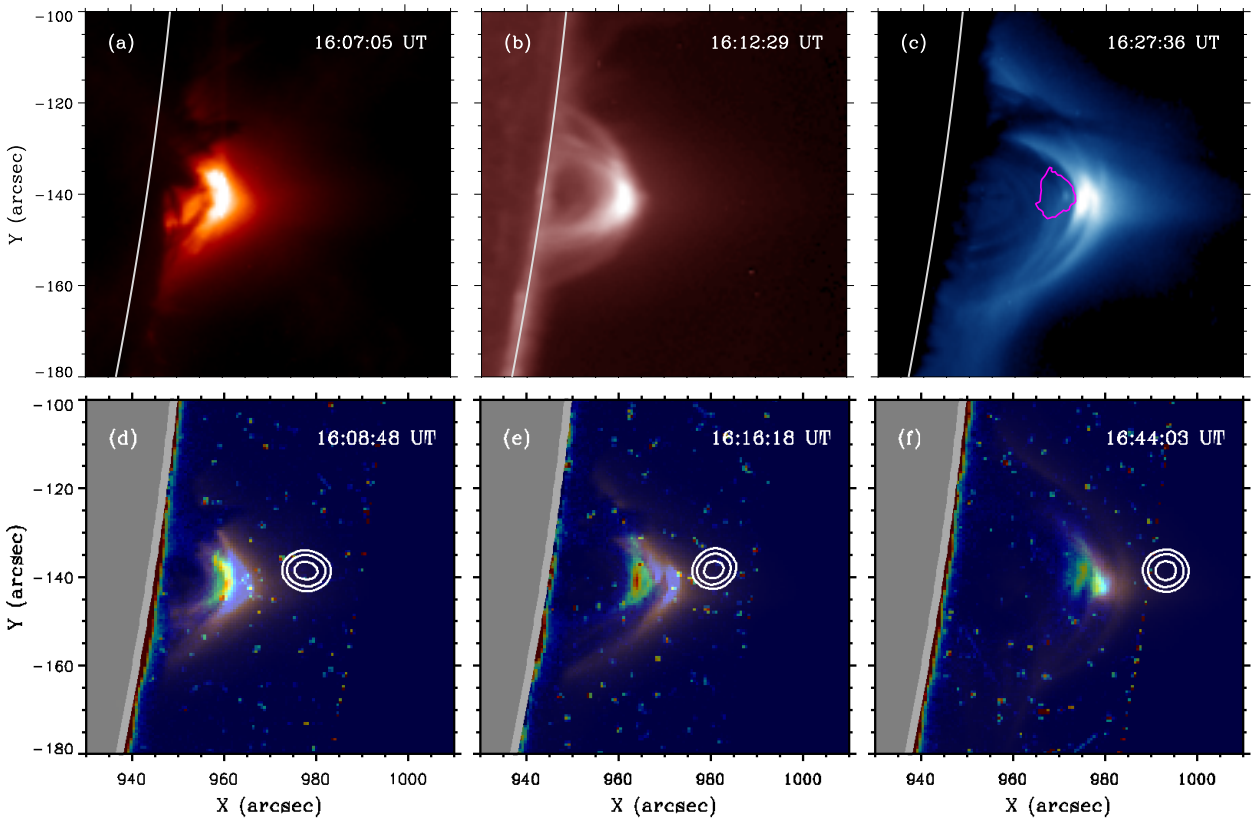

Fig. 2.— Selected images of the flare loops at the wavelength channels of (a) 304 Å near its peak intensity at 16:07:05 UT; (b) 1700 Å near its peak intensity at 16:12:29UT; and (c) 335 Å at 16:27:36UT, overplotted with a magenta WL contour near the WL peak time (see Figure 1e). (d)-(e) Selected composite images of HMI WL (blue-red background image) and AIA 335 Å (orange-white semi-transparent foreground image), with *RHESSI* 10-16 keV intensity over-plotted as white contours.

along with selected composite images showing the relative spatial and temporal relations of WL and EUV channels. Particularly, as seen in Figure 2c, the WL loop-top, at its peak brightness, is located below the 335Å loop-top in its absorption area.

GOES captured the total soft X-ray flux of the Sun in its both channels: 1–8 Å and 0.5–4 Å (Figure 4a). *RHESSI*'s X-ray images did not cover the entire flare event, but its coverage during the early impulsive phase of the flare provides useful information that can be compared with the WL/UV/EUV locations (Figure 3f). Selected *RHESSI* X-ray images are also plotted as contours with the WL and EUV images for comparison of loop-top locations (Figure 2d-f).

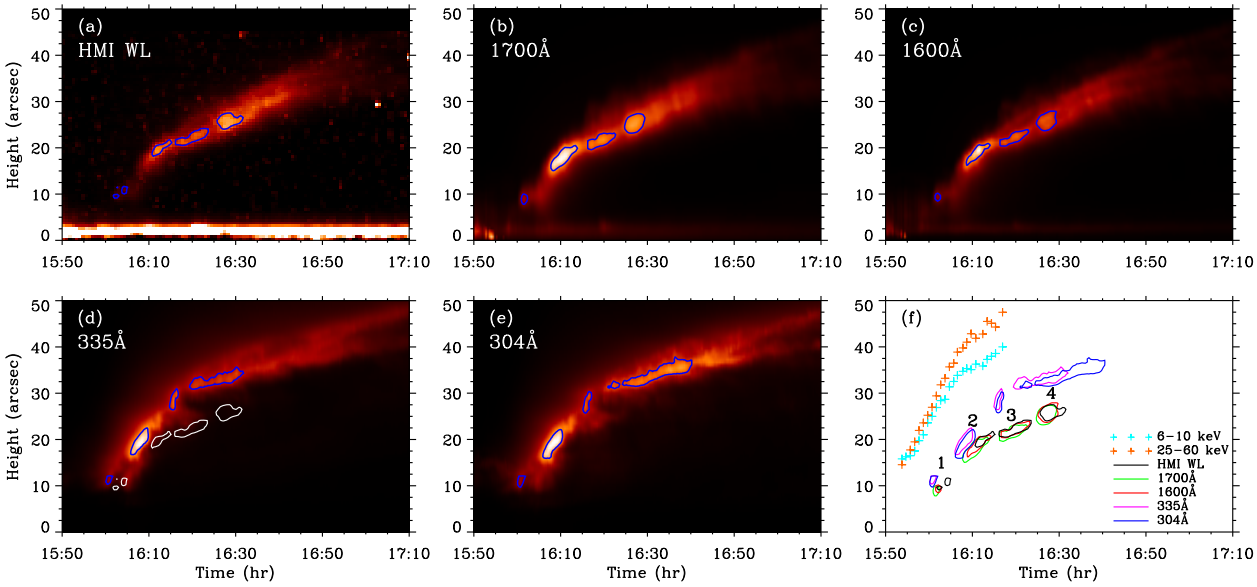

Fig. 3.— Time–height relations obtained for the flare's loop-top after an integration over a $10''$-wide band for each time step, using observations from (a) HMI WL, (b) 1700 Å, (c) 1600 Å, (d) 335 Å, and (e) 304 Å. Contours in each of these images mark the 75% of intensity level at the peak of their corresponding brightness enhancement patches. The WL contours are also plotted in panel (d) to better compare the WL emission relative to EUV emissions. (f) Contours in panels (a) – (e) are plotted together and numbers "1" – "4" are marked corresponding to the four brightening patches. The centroid locations obtained from *RHESSI*'s 6-10 keV and 25-60 keV soft X-ray data are also overplotted as '+' signs for a comparison.

3. Results

3.1. Time–Height Relation

To analyze the time–height relations of the loop-top observed in all the five visible, UV, and EUV channels through the period of interest from 15:56 UT to 17:12 UT, for each time step and for each altitude we integrate the intensity for the total flux in a $10''$-wide band between the dashed lines marked in Figure 1d, which best includes the brightest part of the loop-top. The integrated brightness for all the five wavelength channels, as well as their comparison, are shown in Figure 3 as a function of time and height above the photospheric limb. Note that the HMI, AIA's UV and EUV channels have different temporal cadences of 45 s, 24 s, and 12 s, and HMI and AIA have different pixel sizes of about $0.5''$ and $0.6''$; therefore, the time–height plots in Figure 3 are shown after all the AIA images are interpolated to match the WL image resolution and are aligned with the WL images in space and time.

It can be seen from Figure 3 that through all the five wavelength channels, the loop-top shows four distinct brightness-enhancements patches, each of which is marked by one contour. Within each wavelength channel, every brightness-enhancement patch differs each other in both enhancement amount and duration, therefore we plot the contours using 75% of the peak intensities of their respective patches. As shown in Figure 3f, based on the time and location of the brightness-enhancement patches, the five wavelength channels form two groups, with one group being the WL and UV channels (1700 Å and 1600 Å), and another group the EUV channels (335 Å and 304 Å). Within each group, the height and the duration of the four brightness enhancements observed in different channels are quite similar but do not exactly overlap. The brightness enhancements in the EUV channels occur earlier in time and higher in altitude than those in the WL and UV channels, and the time lags and height differences between the two groups of enhancement patches increase as the flare loop-top evolves to higher altitude. The X-ray centroid locations of the loop-top, obtained from the *RHESSI*'s 6-10 keV and 25-60 keV channels during 15:53UT and 16:17UT, can be found at least $10''$ higher and at least 10 minutes earlier than the AIA's EUV channels (Figure 3f).

To better compare the temporal variations of the intensity for all the WL/UV/EUV channels, we further integrate the time–height diagrams over heights, and study the total flux change over time. In order to focus only on the temporal changes in the loop-top, we integrate the intensity between the heights of $6''$ and $45''$ above the limb, excluding the upper photosphere that keeps elevated brightness throughout the analyzed period in the WL and UV channels. Figure 4b shows all the flux curves, which are normalized to 1.0 at their respective major brightness peak between 16:05 – 16:15 UT. It can be seen that all the UV and EUV channels show similar trend of growth and decay, despite that the UV channels are grouped together with the WL in the brightness-enhancement time and altitude. Showing a growth trend similar to the UV channels before the first major peak around 16:12 UT, the WL light flux continues to grow to a brighter peak around 16:28 UT after a 5-min dip in brightness following the first peak. This can also well be seen in Figure 1 and its accompanied animation. That is, the WL and UV channels show sharply different behaviors after about 16:17 UT despite their many similarities in other aspects, highlighting the different emission mechanisms in the WL and UV wavelengths at the flare's loop-top. For comparison, the *GOES* soft X-ray flux is plotted in Figure 4a. We need to keep in mind that the *GOES* flux is an integration of the X-ray flux of the entire Sun, including the flare's footpoints, loops, and elsewhere, while the fluxes shown in Figure 4b are obtained only from the flare's off-limb loop-top.

3.2. Quasi-Periodic Pulsations

To study the shorter-period pulsations in the brightness observed in all the wavelengths, we detrend the brightness curves shown in Figure 4b by subtracting their respective running averages

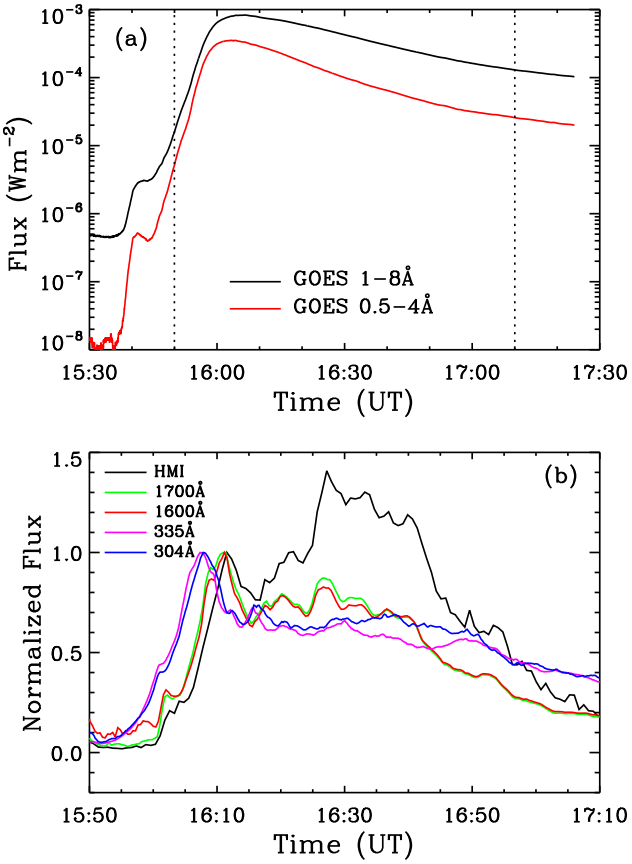

Fig. 4.— (a) Soft X-ray flux from *GOES* during the flare's impulsive and gradual phases. Vertical dotted lines indicate the time window for the curves plotted in panel (b). (b) Temporal evolution of the flux for the HMI and AIA wavelength channels, integrated in the stripe shown in Figure 1e. All fluxes are normalized relative to their respective peak fluxes during 16:05 – 16:15UT.

with a window width of 300 sec, a practice commonly used in studying quasi-periodic pulsations (e.g., Hayes et al. 2019; Yuan et al. 2019). We have experimented with different window widths, and found that the 300-sec window width only suppresses long-period pulsations with little impact on the short-period pulsations that are of interest in this study. The left panels of Figure 5 show the detrended flux curve of the WL and its comparisons with the detrended curves from the UV and EUV channels, and the right panels of Figure 5 show the wavelet power of the detrended curves of the WL, one UV channel (1600 Å), and one EUV channel (335 Å).

It can be seen that both the WL and UV channels show four near-simultaneous brightness peaks, with a seemingly one-to-one correspondence to the four brightness-enhancement patches shown in Figure 3. The WL brightness peaks, marked by the dark arrows, show quasi-periodic pulsations with a period of approximately 8.0 min. The pulsations in the two UV channels occurred

slightly earlier than those in the WL. The wavelet power calculated from the detrended WL flux curves peaks around the period of 8.0 min at the beginning, and gradually shifts to the period of 5 min, lasting a total of about 40 min. The wavelet power calculated from the 1600 Å shows a wider period range between ∼7 and ∼11 min and lasts for about 30 min.

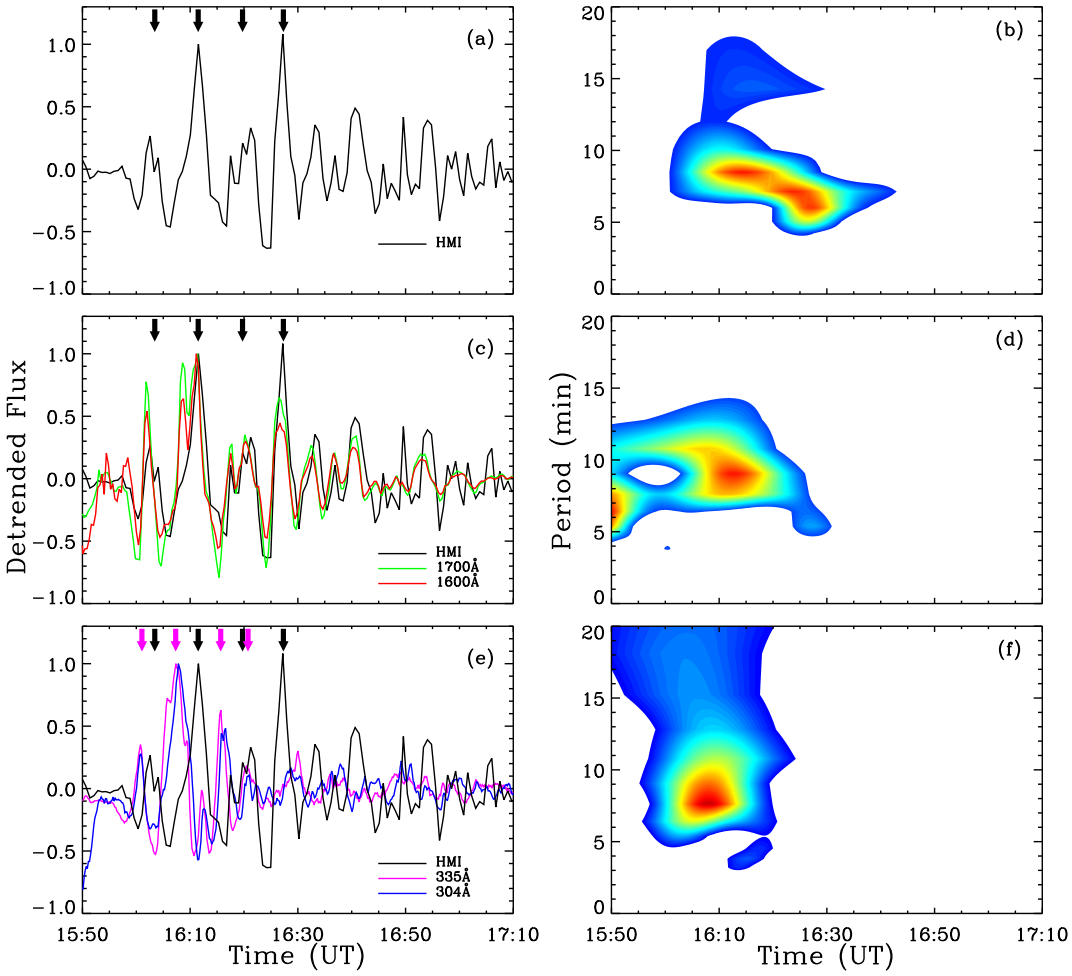

Fig. 5.— (a) Detrended HMI WL flux curve, and (b) wavelet power of the detrended WL curve. (c) Comparison of detrended flux curves between the WL and the UV channels, and (d) wavelet power of the detrended 1600 Å curve. (e) Comparison of detrended flux curves between the WL and the EUV channels, and (f) wavelet power of the detrended 335 Å curve. Dark arrows in the left panels point to the four peak times in the detrended WL curve, and the magenta arrows indicate the peak times of the detrended 335 Å curve. The shown wavelet power maps are part of a map that has a longer time sequence of 2 hr with a longer period range, thus the influence cones locate outside of the plotted range.

The pulsations in the two EUV channels, indicated by the four magenta arrows in Figure 5e, lead the WL pulsations by ∼2.4 – 6.5 min. These EUV pulsations are less regular in periodicity with an averaged period of ∼6.6 min, significantly shorter than that of the WL pulsations. Between the two EUV channels, the pulsations in 335 Å channel lead those in 304 Å channel slightly by about 28 sec, estimated through cross-correlation. It is rather interesting that there are four episodes of emission enhancements across EUV, UV, and WL channels. However, it is not clear whether there exists an one-to-one physical correspondence among the pulsations of these channels, because of their different emission mechanisms and the complex flare structure involving an arcade of loops distributed along the line-of-sight that can contribute to the EUV emission due to its optically-thin nature.

4. Discussion

We have analyzed the rare white-light observation of the evolution of an off-limb loop system in the SOL2017-09-10 X8.2 flare, and found that (1) there are quasi-periodic pulsations in the WL and UV channels with a period of around 8.0 min, and less regular pulsations with an average period of 6.6 min in the EUV channels; (2) intensity-enhancements appear sequentially in WL and UV/EUV channels with time delays and altitude decreases corresponding to progressively lower temperatures of the emitting plasma; and (3) the WL flux of the flare's loop-top continues to grow for about 16 more minutes while the UV/EUV fluxes decay.

The quasi-periodic pulsations observed across the WL/UV/EUV channels, with different periods and irregular time delays between different channels, implies that these pulsations are unlikely of the MHD wave nature or oscillatory properties of the flaring plasma. Through analyzing the evolution of a strong on-disk flare, Asai et al. (2004) suggested that repeated enhancements of X-ray/EUV emissions were indicative of energy release and particle acceleration episodes resulting from magnetic reconnection. Our observation of the limb-flare loop presents a different view angle of a similar phenomenon, whose quasi-periodic brightenings are also possibly caused by episodic magnetic reconnection above. For this same flaring event, Reeves et al. (2021) found damped oscillations in Doppler velocity with a period ∼400 s in the region south of the the main flare arcade, and suggested that the oscillations are caused by magnetic reconnection outflows. Despite different areas of the same event analyzed, the loop-top of the main arcade in our study and the loop-top south of the main arcade in theirs, the similarities in the pulsation periods may point to a common physical cause – pulsed magnetic reconnection.

The brightness-enhancement patches across different wavelengths can serve as tracers of the flare's energy release and subsequent thermodynamic evolution across different temperature and density ranges. As Figure 3f shows, the emission generally progresses with time toward lower alti-

tudes from X-ray to EUV and then UV/WL, corresponding to the emitting plasma at progressively lower temperatures. This is a well-known trend that can result from the interplay of (a) upward development of magnetic reconnection toward higher altitude with time in the standard flare model, (b) downward contraction of newly reconnected hot flaring loops that undergo cooling at the same time. Such contractions have various observational manifestations, such as shrinkage of flare loops (Švestka et al/ 1987) at speeds of the order of 10 km s^{-1} seen in soft X-rays (Forbes & Acton 1996; Reeves et al. 2008), and the so-called supra-arcade downflows (e.g., McKenzie & Hudson 1999; Savage & McKenzie 2011; Liu et al. 2013). In our analysis (see Figure 3f), the altitudes for the first two groups of brightenings, around 16:02UT and 16:10UT across all wavelengths, are similar at about 10″ and 18″ above the limb, while the time delays between the EUV and UV emissions are about 2 and 4 min, respectively. For the other two groups of later brightenings, the EUV emission originates about 7″ higher than the UV/WL emission with time delays of 3 – 5 min, which translates to a speed of $\sim 17 - 28$ km s^{-1} if we assume this results from loop shrinkage. This trend agrees with the increase with time of the separation between the 6-10 and 25-60 keV X-ray emission centroids (especially after about 16:05UT; cf., Liu et al. 2004).

Despite many similarities in WL and UV observations, their integrated light curves show different trends: the WL flux continues to grow while the UV flux starts to decay after the peak around 16:10UT. This implies, unsurprisingly, that the UV and WL have different emission mechanisms. Off-limb flare loops are visible in WL primarily because of a combination of the following processes: hydrogen Paschen and Brackett recombination, hydrogen free-free continuum emission, and Thomson scattering of the solar radiation (Heinzel et al. 2017; Jejčič et al. 2018). It is likely that before 16:10UT plasma temperature is relatively high at the flare's loop-top, and all the WL emission mechanisms play a role. After 16:10UT and above the height of approximately 22″ (see Figure 3a), the temperature may have dropped substantially and resulted in reduced UV/EUV emissions; however, the increasing electron density may still keep the WL intensity growing for a longer time, primarily because the Paschen and Brackett recombination and free-free emission depend quadratically on the density. However, one should also realize that high densities also correspond to non-negligible opacity leading to a decrease of emission. In fact, a detailed comparison of WL and EUV 335Å emissions in Figures 2c and 3d, along with the sequence of 335Å images, shows that during the EUV decay period, the WL emissions are located in an area of reduced 335 Å emission that appears to be a dark absorption. This is also evident on other AIA EUV channels, such as 193Å and 211Å (cf. Figure 1 of Heinzel et al. 2020 and Figure 3 of Jejčič et al. 2018), providing another piece of evidence that plasma has cooled substantially in the areas where WL intensity enhances.

We thank an anonymous referee for constructive comments that helped shape this paper to the current version. Both *SDO* and *RHESSI* are NASA space missions, and *GOES* are NOAA

satellites. J. Z. is partly sponsored by NASA grant 80NSSC18K0668. W. L. was supported by NASA grants NNX16AF78G, 80NSSC21K1327, and 80NSSC21K1687.

REFERENCES

Asai, A., Yokoyama, T., Shimojo, M., & Shibata, K. 2004, ApJ, 605, L77

Brosius, J. W., Daw, A. N., & Inglis, A. R. 2016, ApJ, 830, 101

Dennis, B. R., Tolbert, A. K., Inglis, A. R., et al. 2017, ApJ, 836, 84

Dominique, M., Zhukov, A. N., Dolla, L., et al. 2018, Sol. Phys., 293, 61

Fleishman, G. D., Gary, D. E., Chen, B., Kuroda, N., Yu, S., & Nita, G. M. 2020, Science, 367, 278

Forbes, T. G., & Acton, L. W. 1996, ApJ, 459, 330

Gary, D. E., Chen, B., Dennis, B. R., et al. 2018, ApJ, 863, 83

Hayes, L. A., Gallagher, P. T., Dennis, B. R., Ireland, J., Inglis, A., & Morosan, D. E. 2019, ApJ, 875, 33

Heinzel, P., Kleint, L., Kašparová, J., & Krucker, S. 2017, ApJ, 847, 48

Heinzel, P., Schwartz, P., Lörinčík, J., et al. 2020, ApJ, 896, L35

Hiei, E., Nakagomi, Y., & Takuma, H. 1992, PASJ, 44, 55

Hudson, H. S. 2011, Space Sci. Rev., 158, 5

Hudson, H. S., Wolfson, C. J., & Metcalf, T. R. 2006, Sol. Phys., 234, 79

Jejčič, S., Kleint, L., & Heinzel, P. 2018, ApJ, 867, 134

Kuridze, D., Mathioudakis, M., Morgan, H., et al. 2019, ApJ, 874, 126

Lemen, J. R., Title, A. M., Akin, D. J., et al. 2012, Sol. Phys., 275, 17

Li, D., Ning, Z. J., & Zhang, Q. M. 2015, ApJ, 807, 72

Lin, R. P., Dennis, B. R., Hurford, G. J., et al. 2002, Sol. Phys., 210, 3

Liu, W., Chen, Q., Petrosian, V. 2013, ApJ, 767, 168

Liu, W., Jiang, Y. W., Liu, S., Petrosian, V. 2004, ApJ, 611, L53

Martínez Oliveros, J.-C., Krucker, S., Hudson, H. S., et al. 2014, ApJ, 780, L28

McKenzie, D. E., Hudson, H. S. 1999, ApJ, 519, L93

Murray, M. J., van Driel-Gesztelyi, L., & Baker, D. 2009, A&A, 494, 329

Nakariakov, V. M., Foullon, C., Myagkova, I. N. 2010, ApJ, 708, L47

Nakariakov, V. M., & Melnikov, V. F. 2009, Space Sci. Rev., 149, 119

Pesnell, W. D., Thompson, B. J., & Chamberlin, P. C. 2012, Sol. Phys., 275, 3

Reeves, K. K., Polito, V., Chen, B. Galan, G., Yu, S., Liu, W., & Li, G. 2021, ApJ, 905, 165

Reeves, K. K., Seaton, D. B., & Forbes, T. G. 2008, ApJ, 675, 868

Saint-Hilaire, P., Schou, J., Martínez Oliveros, J.-C., Hudson, H. S., Krucker, S., Bain, H., & Couvidat, S. 2014, ApJ, 786, L19

Savage, S. L., & McKenzie, D. E. 2011, ApJ, 730, 98

Scherrer, P. H., Schou, J., Bush, R. I., et al. 2012, Sol. Phys., 275, 207

Schou, J., Scherrer, P. H., Bush, R. I., et al. 2012, Sol. Phys., 275, 229

Švestka, Z. F., Fontenla, J. M., Machado, M. E., et al. 1987, Sol. Phys., 108, 237

Tian, H., Young, P. R., Reeves, K. K., et al. 2016, ApJ, 823, L16

Van Doorsselaere, T., Kupriyanova, E. G., & Yuan, D. 2016, Sol. Phys., 291, 3143

Warren, H. P., Brooks, D. H., Ugarte-Urra, I., Reep, J. W., Crump, N. A., & Doschek, G. A. 2018, ApJ, 854, 122

Yu, S., Chen, B., Reeves, K. K., et al. 2020, ApJ, 900, 17

Yuan, D., Feng, S., Li, D., Ning, Z., & Tan, B. 2019, ApJ Lett., 886, L25